

Communication

# Enhanced Electrochemical Performance of $\text{Sb}_2\text{O}_3$ as an Anode for Lithium-Ion Batteries by a Stable Cross-Linked Binder

Yong Liu <sup>1,2,\*</sup>, Haichao Wang <sup>1,†</sup>, Keke Yang <sup>1</sup>, Yingnan Yang <sup>1</sup>, Junqing Ma <sup>1</sup>, Kunming Pan <sup>1</sup>, Guangxin Wang <sup>2</sup>, Fengzhang Ren <sup>1</sup> and Huan Pang <sup>3,\*</sup>

<sup>1</sup> Collaborative Innovation Center of Nonferrous Metals of Henan Province, Henan Key Laboratory of High-Temperature Structural and Functional Materials, School of Materials Science and Engineering, Henan University of Science and Technology, Luoyang 471023, China

<sup>2</sup> Henan Key Laboratory of Non-Ferrous Materials Science & Processing Technology, Henan University of Science and Technology, Luoyang 471023, China

<sup>3</sup> School of Chemistry and Chemical Engineering, Yangzhou University, Yangzhou 225009, China

\* Correspondence: liuyong209@haust.edu.cn (Y.L.); panghuan@yzu.edu.cn (H.P.)

† These authors contributed equally to this work.

Received: 26 May 2019; Accepted: 28 June 2019; Published: 30 June 2019



**Abstract:** A binder plays an important role in lithium-ion batteries (LIBs), especially for the electrode materials which have large volume expansion during charge and discharge. In this work, we designed a cross-linked polymeric binder with an esterification reaction of Sodium Carboxymethyl Cellulose (CMC) and Fumaric Acid (FA), and successfully used it in an  $\text{Sb}_2\text{O}_3$  anode for LIBs. Compared with conventional binder polyvinylidene fluoride (PVDF) and CMC, the new cross-linked binder improves the electrochemical stability of the  $\text{Sb}_2\text{O}_3$  anode. Specifically, with CMC-FA binder, the battery could deliver  $\sim 611.4 \text{ mAh g}^{-1}$  after 200 cycles under the current density of  $0.2 \text{ A g}^{-1}$ , while with PVDF or CMC binder, the battery degraded to 265.1 and  $322.3 \text{ mAh g}^{-1}$ , respectively. The improved cycling performance is mainly due to that the cross-linked CMC-FA network could not only efficiently improve the contact between  $\text{Sb}_2\text{O}_3$  and conductive agent, but can also buffer the large volume change of the electrode during repeated charge/discharge cycles.

**Keywords:** cross-linked binder; sodium carboxymethyl cellulose; fumaric acid;  $\text{Sb}_2\text{O}_3$  anode; lithium-ion batteries

## 1. Introduction

Nowadays, advanced energy conversion and storage devices, such as supercapacitor, lithium-ion batteries (LIBs) and solar cells, have gradually become research hotspots to manage the energy supply for future sustainable resources [1–4]. Among them, LIBs have been widely used in almost all aspects of our lives for their high energy density, long life span, and environmental friendliness [5–11]. Although the energy density of LIBs grew very quickly in recent years, it still could not meet people's growing demand. For graphite, the anode material of a commercial lithium battery, the theoretical specific capacity of which is only about  $372 \text{ mAh g}^{-1}$ , and this poses a great obstacle to the increase of lithium ion battery capacity [12–22]. Nevertheless, the post-transition metal oxides (PTMOs) have attracted much attention because of their high theoretical capacity ( $>600 \text{ mAh g}^{-1}$ ) [23], such as  $\text{SnO}_2$  [24],  $\text{Sb}_2\text{O}_3$  [25–27],  $\text{Sb}_2\text{O}_4$  [28] and  $\text{Sb}_6\text{O}_{13}$  [29]. Among these PTMOs,  $\text{Sb}_2\text{O}_3$  has advantages of low cost, simple synthesis process, and easily availability of raw materials, making it a promising electrode material for rechargeable lithium-ion batteries [30]. However, the lithium storage mechanism of  $\text{Sb}_2\text{O}_3$  is found to be phase conversion and alloying, which could cause great volume increases or shrinks

during cycling [23]. Thus, Solid Electrolyte Interphases (SEI), on  $\text{Sb}_2\text{O}_3$  electrode during initial cycle, would be disrupted, exposing new active site and forming new SEI during cycling, resulting in a decrease in capacity [31].

To stabilize an  $\text{Sb}_2\text{O}_3$  electrode, many researchers have been working on controlling the morphology of  $\text{Sb}_2\text{O}_3$ , such as synthesizing porous  $\text{Sb}_2\text{O}_3$  [32] and  $\text{Sb}_2\text{O}_3$  nanowires [33], and decorating  $\text{Sb}_2\text{O}_3$  with different carbon materials; for instance, carbon cloth [34], reduced graphene oxide [35] and so on. Even though these methods can improve the electrochemical performance of  $\text{Sb}_2\text{O}_3$  electrodes, the synthesis processes are complex and of high cost, which limits their wide application. Moreover, the addition of carbon material will reduce the specific capacity of the electrode.

A binder plays a crucial role in affecting the performance of LIBs. Compared to traditional linear binder, cross-linked binder not only could improve the binding between active material and conductive agent, but also can accommodate volume expansion of the electrode during cycling [36–38]. The construction of three-dimensional crosslinking structure can improve the cycling stability of the battery, which has been described in many studies [38,39]. For example, Song and his colleagues obtained enhanced electrochemical performance of Si anode for lithium-ion batteries by using a PAA-PVA polymeric binder [39]. Recently, Liu et al. synthesized a stable cross-linking polymeric network of CMC and citric acid (CA) and used it in silicon-based anodes of LIBs, in which an enhanced cycling stability was obtained comparing to linear polymeric PVDF and CMC binders [36]. Moreover, a more stable silicon electrode was also obtained by designing corn starch–maleic anhydride cross-linked binder [40]. In these studies, various novel binder systems for stabilizing the silicon anode for LIBs were fabricated, enhancing their cycling stability.

It is known that Si and  $\text{Sb}_2\text{O}_3$  are similar alloying mechanism in degradation of capacity during repeated lithium ion insertion/extraction [38,41]. In this work, we designed a cross-linked polymeric binder with esterification reaction of CMC and Fumaric Acid (FA), and successfully applied it in  $\text{Sb}_2\text{O}_3$  anode for LIBs. Compared with conventional binder PVDF and CMC, the cross-linked CMC-FA polymeric network effectively enhanced the  $\text{Sb}_2\text{O}_3$  anode electrochemical performance in LIBs. Specifically, with CMC-FA binder, the battery could deliver  $\sim 611.4 \text{ mAh g}^{-1}$  (200 cycles,  $0.2 \text{ A g}^{-1}$ ), while with PVDF and CMC, the battery degraded to 265.1 and  $322.3 \text{ mAh g}^{-1}$ , respectively. This effective solution for enhancing cycling stability of  $\text{Sb}_2\text{O}_3$  in LIBs is simple and inexpensive, and could facilitate the commercialization of  $\text{Sb}_2\text{O}_3$  for LIBs.

## 2. Materials and Methods

### 2.1. Synthesis of $\text{Sb}_2\text{O}_3$ Sample

$\text{Sb}_2\text{O}_3$  particles were synthesized through a self-propagating room temperature reaction method as described elsewhere [42]. Specifically, solutions with 3.310 g  $\text{SbCl}_3$  and 4.940 g NaOH in 40 mL distilled water were prepared separately. Then, NaOH solution was slowly added to  $\text{SbCl}_3$  solution (Operator should wear goggles and mask to prevent high temperature chemical liquid splashing). After stirring in beaker for several minutes, the solution was sealed; 3 h later, the obtained slurry was centrifuged and rinsed repeatedly with distilled water to dissolve the excess of NaOH. Finally, the  $\text{Sb}_2\text{O}_3$  particle was obtained after 8 h of drying in the vacuum oven at  $60^\circ\text{C}$ .

### 2.2. Materials Characterization

The crystalline structure of the as-synthesized samples was characterized by X-ray diffraction (XRD, Bruker D8 ADVANCE,  $\text{Cu } \alpha$  source), and the microstructures and morphology were observed by scanning electron microscope (SEM, JSM-5610LV, JEOL, Akishima, Japan), and transmission electron microscope (TEM, JSM-2100F, 200 kV, Hitachinaka, Naka, Japan) and high-resolution transmission electron microscope (HRTEM, FEI, TecnaiG2 F30, 200kV, Hitachinaka, Naka, Japan). The sample of cross-linked binder (CMC-FA) was prepared by the method same as preparing electrode without active materials and conductive materials, Fourier transform infrared (FT-IR) spectrascopy of CMC,

FA and CMC-FA samples were carried out as diffuse reflectance measurements using a Bruker IFS 66/S FT-IR spectrometer and Spectra-Tech Collector II DRIFTS accessory. The specific surface area of the sample was calculated based on Brunauer–Emmett–Teller (BET) method through nitrogen gas adsorption isotherms measured by using a BEL mini instrument.

### 2.3. Preparation of Electrodes

The  $\text{Sb}_2\text{O}_3$  electrodes using polyvinylidene fluoride (PVDF 5130, Solvay), Sodium Carboxymethyl Cellulose (CMC) and cross-linked Carboxymethyl Cellulose-Fumaric Acid (CMC-FA) as binders, were denoted as PVDF@ $\text{Sb}_2\text{O}_3$ , CMC@ $\text{Sb}_2\text{O}_3$  and CMC-FA@ $\text{Sb}_2\text{O}_3$ , respectively. The electrode slurry was prepared by mixing active materials ( $\text{Sb}_2\text{O}_3$ ), conductive materials (Super P, Shenzhen Kejingstar Technology LTD) and binder with a weight ratio of 6:2:2. The electrode was made by pasting the formed slurry on Cu foil and drying the anode in a vacuum oven at 80 °C for 8 h. For PVDF/CMC@ $\text{Sb}_2\text{O}_3$  electrode, the binder was PVDF or CMC, and the solvent was N-Methyl-2-pyrrolidone (NMP) or deionized water, respectively. For CMC-FA@ $\text{Sb}_2\text{O}_3$  electrode, the weight ratio of CMC:FA was 1:1, and the solvent was Dimethyl sulfoxide (DMSO). Different from PVDF/CMC@ $\text{Sb}_2\text{O}_3$  electrode, CMC-FA@ $\text{Sb}_2\text{O}_3$  electrode was dried at room temperature for 8 h in a vacuum oven and further thermally treated at 150 °C for 2 h to guarantee the esterification reaction between CMC and FA. The electrodes were cut into a 12 mm diameter disk, with a load of around 1–1.2 mg (0.9–1.06 mg cm<sup>-2</sup>) per disk, for electrochemical measurements.

### 2.4. Electrochemical Measurement

In order to evaluate electrochemical performance, CR2025-type coin cells were assembled in an Ar-filled glove box with low concentrations of water vapor and oxygen (<0.5 ppm). During assembly, as-prepared electrodes were used as cathodes, Lithium foil as anode, Celgard 2300 as separator, and the electrolyte was 1 M  $\text{LiPF}_6$  in ethylene carbonate (EC) and diethyl carbonate (DEC) with volume ratio 1:1. The electrochemical lithium storage performance were evaluated through a two-electrode system, in which lithium foil was employed as the counter and reference electrode, and the  $\text{Sb}_2\text{O}_3$  electrodes were employed as working electrode. The galvanostatic charge–discharge performance were evaluated by a LAND battery-testing system (CT2001A, Wuhan, China) between 0.01–3.0 V vs.  $\text{Li}/\text{Li}^+$ . Electrochemical impedance spectroscopy (EIS) was conducted ranging from 100 kHz to 0.01 Hz, and cyclic voltammetry was carried out in the range of 0.01–3.0 V (vs.  $\text{Li}/\text{Li}^+$ ) at a scan rate of 0.2 mV s<sup>-1</sup>. The above two electrochemical tests were carried out on an electrochemical workstation (CHI 660E).

## 3. Results

### 3.1. Material Characterization

The crystallographic phase of the synthesized  $\text{Sb}_2\text{O}_3$  was characterized by X-ray diffraction, and the XRD pattern is depicted in Figure 1a, in which all the strong and sharp peaks are consistent with standard pattern of the Orthorhombic  $\text{Sb}_2\text{O}_3$  phase (JCPDS card No. 71-0383), indicating the high crystalline  $\text{Sb}_2\text{O}_3$  was obtained. Figure 1b shows the SEM image of  $\text{Sb}_2\text{O}_3$ , it is clear that this product is in cuboid-like shape with sizes of 200–400 nm in width and 0.6–2 μm in length, and the cuboid particles easily aggregated together to form bigger particles. The HRTEM image of the as-prepared  $\text{Sb}_2\text{O}_3$  was exhibited in Figure 1c, the interplanar spacing is ~3.15 Å, this corresponds to the spacing between the (121) planes of Antimony Oxide. This is consistent with the X-ray diffraction pattern, as shown in Figure 1a.

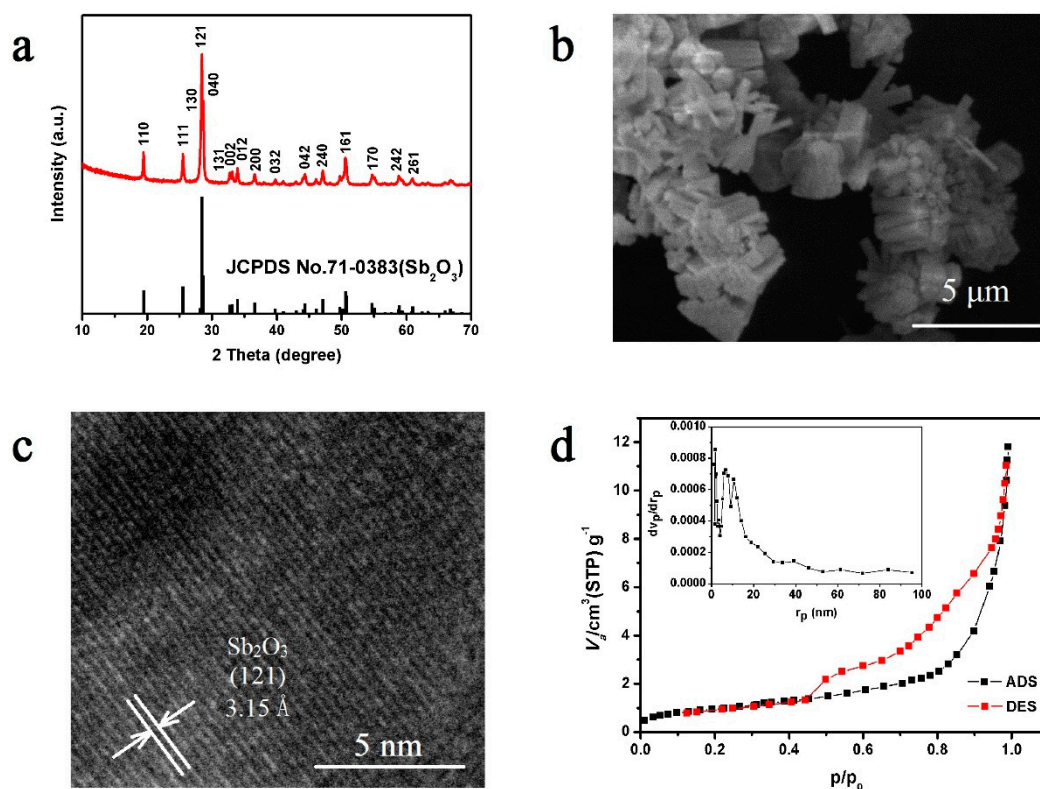


**Figure 1.** Characterization of as-synthesized  $\text{Sb}_2\text{O}_3$  sample: (a) X-ray diffraction patterns; (b) scanning electron microscope image; (c) high-resolution transmission electron microscope image; (d) Nitrogen adsorption-desorption isothermal diagram and Barrett–Joyner–Halenda Plot (inset).

The  $\text{Sb}_2\text{O}_3$  sample was also characterized by Nitrogen adsorption–desorption isotherm measurement, and a typical IV-type isotherm was obtained, as shown in Figure 1d, indicating that there are nearly no micropores existing in the  $\text{Sb}_2\text{O}_3$  sample [43]. A large amount of mesopores (most diameters are less than 40 nm) could be observed in the pore-size distribution curve (inset in Figure 1d). Moreover, the hysteresis hoop of isotherms ascribes that the  $\text{Sb}_2\text{O}_3$  aggregated and formed a slit, consisting with SEM image of  $\text{Sb}_2\text{O}_3$  particles [44]. According to the BET equation and Barrett–Joyner–Halenda (BJH) Plot, the specific surface area of the  $\text{Sb}_2\text{O}_3$  sample was  $\sim 3.42 \text{ m}^2 \text{ g}^{-1}$ .

Figure 2a presents the formation process of cross-linking CMC-FA network by CMC and FA through the esterification reaction. A cross-linking CMC-FA network was formed via the condensation process of the hydroxyl group of CMC and carboxyl group of FA. To identify this chemical reaction, between CMC and FA, the FT-IR measurement was carried out (Figure 2b). For the FA spectrum, the hydroxyl bond dominates the range from  $3700$  to  $2800 \text{ cm}^{-1}$ , and the absorption band between  $3200$  and  $2800 \text{ cm}^{-1}$  could be ascribed to hydroxyl bond between  $-\text{COOH}$  groups of FA [45]. By contrast, for the spectrum of CMC-FA, the nearly disappeared band between  $3200$  and  $2800 \text{ cm}^{-1}$  indicates that the hydroxyl bond in carboxyl of FA was greatly weakened after the cross-linking reaction with CMC and  $\sim 3400 \text{ cm}^{-1}$  has a broad peak which may be attributed to the residual hydroxyl bond of CMC. Moreover, the FT-IR spectra in Figure 2b showed that the  $\text{C}=\text{O}$  band in  $-\text{COOH}$  of FA shifted from  $1677 \text{ cm}^{-1}$  to  $1681 \text{ cm}^{-1}$ , which could be ascribed to an ester group formed via cross linking during condensation reaction between FA and CMC [37]. This esterification reaction of the binders in the electrode could form a cross-linked polymeric network, which could increase the connection within the electrode ( $\text{Sb}_2\text{O}_3$ , Super P, binder and Cu foil). At the same time, it provides an accommodation for the volume change of the  $\text{Sb}_2\text{O}_3$  electrode.

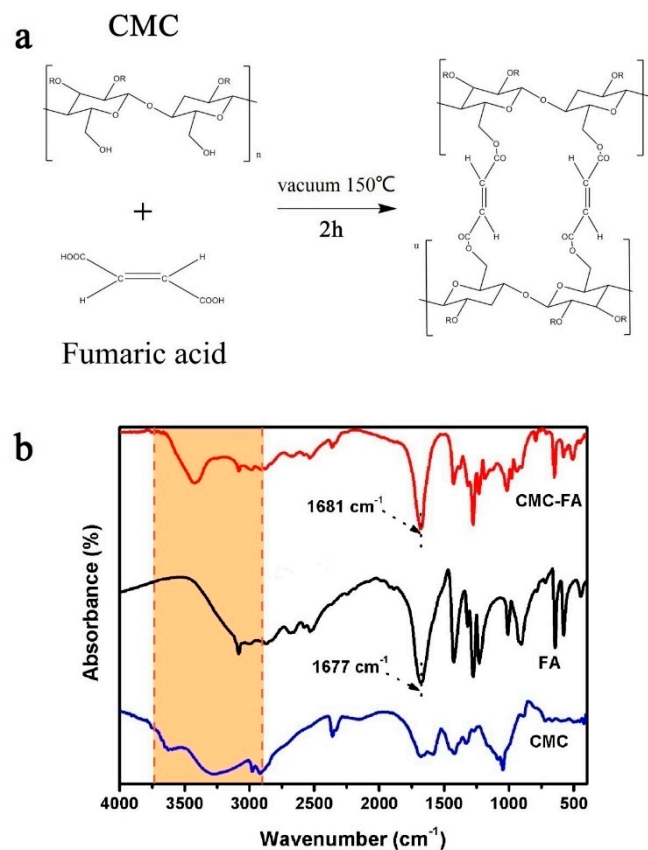


**Figure 2.** (a) The schematic of esterification reaction between CMC and FA; (b) FTIR spectra of FA, CMC and CMA-FA polymer network.

### 3.2. Electrochemical Properties

The cyclic voltammetry (CV) of PVDF@Sb<sub>2</sub>O<sub>3</sub> and CMC@Sb<sub>2</sub>O<sub>3</sub> electrode at a scan rate of 0.2 mV s<sup>-1</sup> between 0.01 V and 3 V was depicted in Figure 3a,b. Both PVDF@Sb<sub>2</sub>O<sub>3</sub> and CMC@Sb<sub>2</sub>O<sub>3</sub> electrodes have similar curves so that the cathodic peaks located at about 1 V could be assigned to the lithiation of Sb<sub>2</sub>O<sub>3</sub> ( $6\text{Li}^+ + \text{Sb}_2\text{O}_3 + 6\text{e}^- \rightarrow 2\text{Sb} + 3\text{Li}_2\text{O}$ ) during the first cycle [23,46], and the following reduction peaks at about 0.6 V may be associated with the multi-step lithiation of Sb ( $6\text{Li}^+ + 2\text{Sb} + 6\text{e}^- \rightarrow 2\text{Li}_3\text{Sb}$ ). The shift from ~0.8 V to ~1.5 V in the subsequent reduction peaks show an activation procedure in the initial lithium-ion insertion process [23]. As for oxidation peaks, the peaks centered at about 1.2 V and 1.5 V may be caused by de-alloying process ( $2\text{Li}_3\text{Sb} \rightarrow 6\text{Li}^+ + 2\text{Sb} + 6\text{e}^-$ ). As for the CV curves of CMC-FA@Sb<sub>2</sub>O<sub>3</sub> electrode in Figure 3c, some characteristic peaks were detected where the triangle notation in the figure was caused by lithiation and delithiation process as described above. In addition, those extra reduction peaks and distorted oxidation peaks may be attributed to some side reactions under the effect of CMC-FA polymer network.

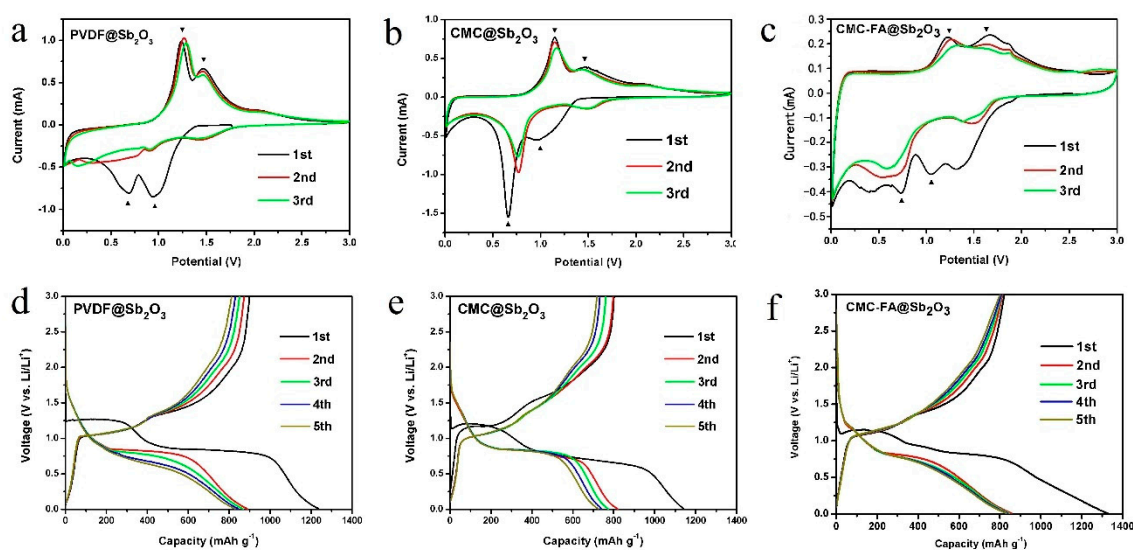


**Figure 3.** (a–c) Cyclic voltammetry curves of PVDF@Sb<sub>2</sub>O<sub>3</sub>, CMC@Sb<sub>2</sub>O<sub>3</sub> and CMC-FA@Sb<sub>2</sub>O<sub>3</sub> at scan rate of 0.2 mV s<sup>-1</sup>; (d–f) galvanostatic charge-discharge profiles of PVDF@Sb<sub>2</sub>O<sub>3</sub>, CMC@Sb<sub>2</sub>O<sub>3</sub> and CMC-FA@Sb<sub>2</sub>O<sub>3</sub> in the initial five cycles at 0.2 A g<sup>-1</sup>.

As the Figure 3d–f shows, the lithiation/delithiation plateaus of the PVDF@Sb<sub>2</sub>O<sub>3</sub>, CMC@Sb<sub>2</sub>O<sub>3</sub> and CMC-FA@Sb<sub>2</sub>O<sub>3</sub> at 0.2 A g<sup>-1</sup>, were nearly consistent with the peaks in the cyclic voltammetry curve. The initial discharge capacity of CMC-FA@Sb<sub>2</sub>O<sub>3</sub> is 1315.8 mAh g<sup>-1</sup>, which is higher than PVDF@Sb<sub>2</sub>O<sub>3</sub> (1236 mAh g<sup>-1</sup>) and CMC@Sb<sub>2</sub>O<sub>3</sub> (1141.3 mAh g<sup>-1</sup>). The initial coulombic efficiency of PVDF@Sb<sub>2</sub>O<sub>3</sub>, CMC@Sb<sub>2</sub>O<sub>3</sub> and CMC-FA@Sb<sub>2</sub>O<sub>3</sub> is 72.73%, 70.24% and 60.09%, respectively. The low coulombic efficiency of three electrodes may be attributed to a form of SEI and conversion reaction of Sb<sub>2</sub>O<sub>3</sub> [47]. In addition, the charge–discharge curves in the second to fifth cycles of CMC-FA@Sb<sub>2</sub>O<sub>3</sub> overlapped obviously, while the curves of PVDF@Sb<sub>2</sub>O<sub>3</sub> and CMC@Sb<sub>2</sub>O<sub>3</sub> dispersed, indicating that electrodes will have higher cycling stability with the CMC-FA polymer network.

The cycling performances of PVDF@Sb<sub>2</sub>O<sub>3</sub>, CMC@Sb<sub>2</sub>O<sub>3</sub> and CMC-FA@Sb<sub>2</sub>O<sub>3</sub> as anode materials at current density of 0.2 A g<sup>-1</sup> were depicted in Figure 4a. During the first 50 cycles, the specific discharge capacity of CMC-FA@Sb<sub>2</sub>O<sub>3</sub> gradually decreases to 400.5 mAh g<sup>-1</sup>, which may be attributed to some side reactions during the discharge stage of CMC-FA@Sb<sub>2</sub>O<sub>3</sub> electrode (CMC-FA polymer binder has residual hydroxyl group, which may react with PF<sub>5</sub> in electrolyte) [38]. From the 50th cycle, the discharge curve CMC-FA@Sb<sub>2</sub>O<sub>3</sub> goes upward, after 200 cycles, the specific discharge capacity of CMC-FA@Sb<sub>2</sub>O<sub>3</sub> gradually increases to 611.4 mAh g<sup>-1</sup>. The upward trend may be attributed to the activation of CMC-FA@Sb<sub>2</sub>O<sub>3</sub> electrode, some active sites were covered for the reason of as-prepared Sb<sub>2</sub>O<sub>3</sub> particles are easily aggregate, which we have discussed in SEM image and Nitrogen adsorption–desorption isotherms measurement of Sb<sub>2</sub>O<sub>3</sub> particle. Changes in the volume of Sb<sub>2</sub>O<sub>3</sub> particle during lithiation/delithiation may lead to exposure of new active sites and result in capacities increasing. In contrast, the specific discharge capacity of PVDF@Sb<sub>2</sub>O<sub>3</sub> and CMC@Sb<sub>2</sub>O<sub>3</sub> decreases to 286.3 and 272.3 mAh g<sup>-1</sup> after 200 cycles, respectively. The abnormal cycling performance and coulomb efficiency of PVDF@Sb<sub>2</sub>O<sub>3</sub> after 150 cycles may be caused by the collapse of the electrode structure with shedding of active materials. The excellent cycling stability of CMC-FA@Sb<sub>2</sub>O<sub>3</sub> electrode may be ascribed to that the cross-linking network could reinforce the electrode, as well as accommodate the volume change of the electrode in repeated lithiation and delithiation process.

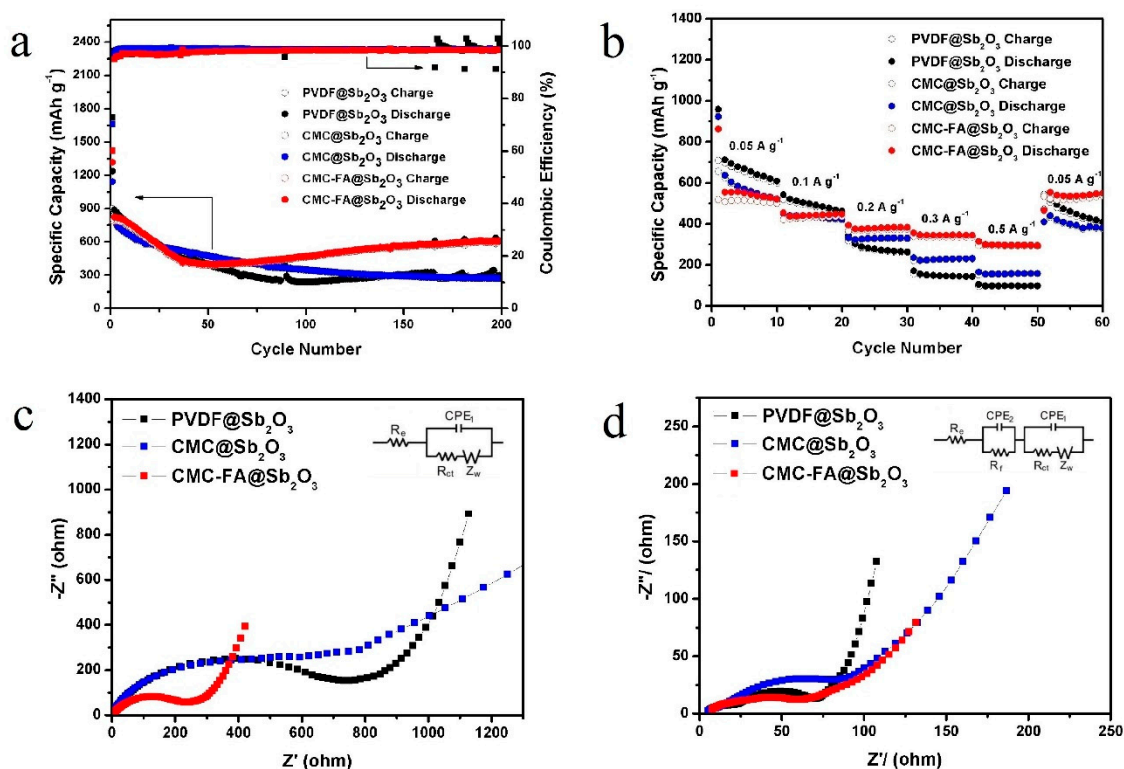


**Figure 4.** (a) Cycling performances of CMC-FA@Sb<sub>2</sub>O<sub>3</sub>, PVDF@Sb<sub>2</sub>O<sub>3</sub> and CMC@Sb<sub>2</sub>O<sub>3</sub> at 0.2 A g<sup>-1</sup>; (b) Rate capabilities of CMC-FA@Sb<sub>2</sub>O<sub>3</sub>, PVDF@Sb<sub>2</sub>O<sub>3</sub> and CMC@Sb<sub>2</sub>O<sub>3</sub> at current density ranging from 0.05 A g<sup>-1</sup> to 0.5 A g<sup>-1</sup>; Nyquist plots of different electrodes: (c) before cycling; (d) after 200 cycles at current density of 0.2 A g<sup>-1</sup>, inset shows electrochemical impedance spectroscopy (EIS) test circuitry.

Figure 4b shows the rate capabilities of PVDF@Sb<sub>2</sub>O<sub>3</sub>, CMC@Sb<sub>2</sub>O<sub>3</sub> and CMC-FA@Sb<sub>2</sub>O<sub>3</sub> at current density ranging from 0.05 to 0.5 A g<sup>-1</sup>. At a current density of 50 and 100 mA g<sup>-1</sup>, capacity of CMC-FA@Sb<sub>2</sub>O<sub>3</sub> is lower than PVDF@Sb<sub>2</sub>O<sub>3</sub> and CMC@Sb<sub>2</sub>O<sub>3</sub> under low current density. This may be due to the slow activation of electrodes under the effect of aggregated Sb<sub>2</sub>O<sub>3</sub> and CMC-FA binder. PVDF@Sb<sub>2</sub>O<sub>3</sub> and CMC@Sb<sub>2</sub>O<sub>3</sub> have same downward trends even though they have higher specific discharge capacity than CMC-FA@Sb<sub>2</sub>O<sub>3</sub>, whose specific discharge capacity is relatively stable. When current density was increased to 0.2, 0.3 and 0.5 A g<sup>-1</sup>, the reversible capacities of CMC-FA@Sb<sub>2</sub>O<sub>3</sub> were 382.9, 344.3 and 295.4 mAh g<sup>-1</sup>, respectively, which is better than PVDF@Sb<sub>2</sub>O<sub>3</sub> and CMC@Sb<sub>2</sub>O<sub>3</sub>. Moreover, when the current density returns to the initial, the capacity of CMC-FA@Sb<sub>2</sub>O<sub>3</sub> could recover to ~569 mAh g<sup>-1</sup>, implying the good rate capability.

The EIS measurements were conducted to test the electrochemical kinetics of different kinds of electrodes, and the test frequencies ranged from 0.1 to 100 kHz. Figure 4c,d show the Nyquist plots of three kinds of electrodes in initial states and after 200 cycles at 0.2 A g<sup>-1</sup>, respectively. The equivalent circuit (inset in Figure 4c,d) was obtained using Nova software. For the impedance spectra before the discharge as shown in Figure 4c, the semicircles in the high-frequency region correspond to charge-transfer resistance ( $R_{ct}$ ) in the interface of electrodes and electrolyte, and the inclined lines in the low frequency region are attributed to insertion of lithium-ions into the negative electrode [48].  $R_e$  was the internal resistance of the as-assembled cell,  $CPE_1$  represents constant phase element of the electrode/electrolyte interface, and  $Z_w$  represents the Warburg impedance. The  $R_{ct}$  of the initial CMC-FA@Sb<sub>2</sub>O<sub>3</sub> electrode is ~269  $\Omega$ , and the PVDF@Sb<sub>2</sub>O<sub>3</sub> and CMC@Sb<sub>2</sub>O<sub>3</sub> are about 733 and 593  $\Omega$ , respectively, much larger than the CMC-FA@Sb<sub>2</sub>O<sub>3</sub>. It can be seen in Figure 4d that in the impedance spectra after 200 cycles, the semicircle in the high frequency region corresponds to the resistance of SEI film, and the semicircle at middle frequency correspond to  $R_{ct}$ , the inclined line at low frequency reflections are attributed to insertion of lithium-ions into the negative electrode [49]. The meaning of

$R_f$  and  $CPE_2$  in equivalent circuits were corresponding to the resistance and constant phase element of the SEI film. As we can see, although the discharge capacity of CMC-FA@ $Sb_2O_3$  electrode is much higher than the other two electrodes after 200 cycles at  $0.2 \text{ A g}^{-1}$  (Figure 4a), they have quite similar overall impedance after 200 cycles, which could be ascribed to the Li anode contribution; the anode SEI film impedance and the anode charge-discharge resistance may have obvious change during cycling [50]. The  $R_{ct}$  decreased to  $\sim 55 \Omega$ ,  $\sim 74.6 \Omega$  and  $90.1 \Omega$  for CMC-FA@ $Sb_2O_3$ , PVDF@ $Sb_2O_3$ , CMC@ $Sb_2O_3$  electrodes, respectively. This fact confirms that the CMC-FA binder could not only increase the connection within the electrode ( $Sb_2O_3$ , super p, binder and Cu foil), but also reduce the particle shedding due to volume changes of  $Sb_2O_3$  electrode during cycling, enhancing the electrode's electrochemical performance.

To further illustrate the performance of the binder, the morphology of electrodes was examined before and after 200 cycles at  $0.2 \text{ A g}^{-1}$ , as depicted in Figure 5. The morphologies of different electrodes before cycling were shown in Figure 5a–c, in which they exhibited similar morphology. Interestingly, a flower-like polymer network could be found in Figure 5c, which may be associated with cross-linking reactions. After 200 cycles, it can be easily found that there are many large cracks and pulverization in the PVDF@ $Sb_2O_3$  electrode and CMC@ $Sb_2O_3$  electrode, shown in Figure 5d,e. As a comparison, the CMC-FA@ $Sb_2O_3$  electrode has better structure integrity with smaller cracks as shown in Figure 5f, so that CMC-FA@ $Sb_2O_3$  has better cycling stability at same charge/discharge conditions. This result indicates that CMC-FA polymer network can mitigate the strain caused by lithiation/delithiation during cycling (Figure 6).

Furthermore, we have compared the electrochemical properties of the CMC-FA@ $Sb_2O_3$  electrode with a reported study on  $Sb_2O_3$ -based composites as anodes for LIBs in Table 1. First, the Synthesis of the  $Sb_2O_3$  sample and cross-linked polymeric binder have the advantages of cheap raw materials, simple reaction and short reaction time, which can greatly reduce the production cost. Second, the superior capacity and long-term cycling performance of CMC-FA@ $Sb_2O_3$  can be explained as that CMC-FA polymer network could improve the integrity of electrode and could buffer the strain caused by volume change of  $Sb_2O_3$  during the recharging process.

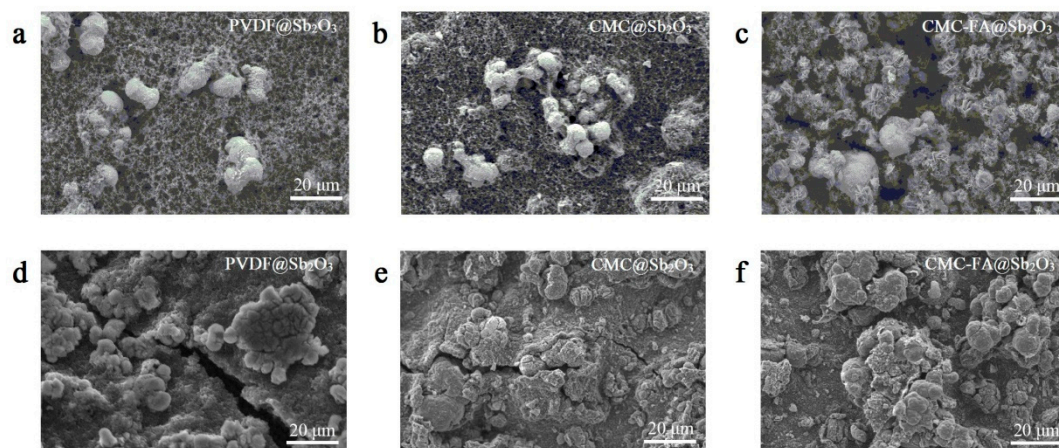


**Figure 5.** SEM images of electrodes before cycling: (a) PVDF@ $Sb_2O_3$ , (b) CMC@ $Sb_2O_3$ , (c) CMC-FA@ $Sb_2O_3$ ; SEM images of electrodes after 200 cycles at current density of  $200 \text{ mAh g}^{-1}$ : (d) PVDF@ $Sb_2O_3$ , (e) CMC@ $Sb_2O_3$ , (f) CMC-FA@ $Sb_2O_3$ .

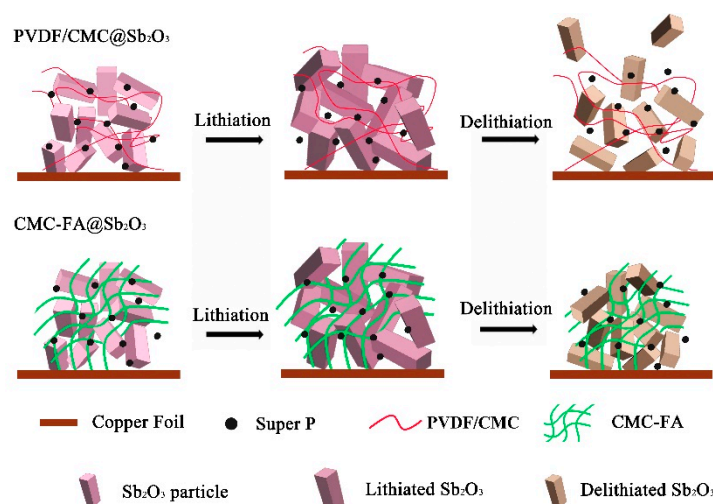


**Figure 6.** Schematic illustration of the proposed mechanism of cross-linked CMC-FA binder and PVDF/CMC binder in  $\text{Sb}_2\text{O}_3$  electrodes.

**Table 1.** Comparison of the electrochemical performances of  $\text{CMC-FA@Sb}_2\text{O}_3$  with previously reported  $\text{Sb}_2\text{O}_3$ -based composites as anode materials for lithium ion batteries.

Materials	Current Density (mA/g)	Cycle Number	Specific Capacity (mAh/g)	Ref
octahedral $\text{Sb}_2\text{O}_3$	200	50	640.8	[30]
carbon-coated $\text{Sb/Sb}_2\text{O}_3$	100	100	686	[51]
hollow $\text{Sb}_2\text{O}_3/\text{TiO}_2$	100	100	593	[52]
bundle shaped $\text{Sb}_2\text{O}_3$	20	100	594.1	[25]
3D nest-shaped $\text{Sb}_2\text{O}_3/\text{RGO}$ composites	50	100	562	[53]
$\text{CMC-FA@Sb}_2\text{O}_3$	200	200	611.4	This work

#### 4. Conclusions

In conclusion, we successfully designed a cross-linked polymeric binder through esterification reaction of CMC and FA and used it in  $\text{Sb}_2\text{O}_3$  for LIBs. It was found that  $\text{CMC-FA@Sb}_2\text{O}_3$  electrodes exhibited good cycling stability and rate capability, better than the electrodes with conventional binder. The results are ascribed to that the novel binder could improve the connection between active materials, conductive agent, and current collector, and also could accommodate the volume expansion of the  $\text{Sb}_2\text{O}_3$  anode in the cycles. Further studies will probably focus on preventing side reactions, improving the cycling stability of initial cycles and solving the aggregation of  $\text{Sb}_2\text{O}_3$  by decorating with functional materials, which may reduce the activation time and improve the early cycling performance of the  $\text{CMC-FA@Sb}_2\text{O}_3$  electrode. Furthermore, this low-cost cross-linked binder may be generalized to other electrode materials for lithium ion batteries, which suffer from large volume-changes during cycling.

**Author Contributions:** Y.L., F.R. and H.P. conceived and designed the experiments; H.W., K.Y. and Y.Y. performed the experiments; H.W., J.M. and K.P. analyzed the data; H.W. wrote the paper, Y.L. and G.W. revised the paper. All the authors have discussed the results and commented on the manuscript.

**Funding:** This work was supported by Program for Changjiang Scholars and Innovative Research Team in University (IRT\_16R21), the Chinese 02 Special Fund (2017ZX02408003), the Key Research Projects of Colleges and Universities in the Henan Province (15A430023), the Scientific and Technological Project of Henan Province (182102210297), Open Fund of National Joint Engineering Research Center for abrasion control and molding of metal materials (HKDNM201802, HKDNM201807), Scientific Research Starting Foundation for Ph.D. of Henan University of Science and Technology (13480065), Science Foundation for Youths of Henan University of Science and Technology (2013QN006) and the Student Research Training Plan of Henan University of Science and Technology (2018029).

**Conflicts of Interest:** The authors declare no conflict of interest.

## References

1. Chu, S.; Cui, Y.; Liu, N. The path towards sustainable energy. *Nat. Mater.* **2017**, *16*, 16–22. [[CrossRef](#)] [[PubMed](#)]
2. Armand, M.; Tarascon, J.M. Building better batteries. *Nature* **2008**, *451*, 652–657. [[CrossRef](#)] [[PubMed](#)]
3. Larcher, D.; Tarascon, J.M. Towards greener and more sustainable batteries for electrical energy storage. *Nat. Chem.* **2015**, *7*, 19–29. [[CrossRef](#)] [[PubMed](#)]
4. Liu, Y.; Zhai, X.L.; Yang, K.K.; Wang, F.; Wei, H.J.; Zhang, W.H.; Ren, F.Z.; Pang, H. Mesoporous NH<sub>4</sub>NiPO<sub>4</sub> center dot H<sub>2</sub>O for High-Performance Flexible All-Solid-State Asymmetric Supercapacitors. *Front. Chem.* **2019**, *7*, 118. [[CrossRef](#)] [[PubMed](#)]
5. Suga, T.; Konishi, H.; Nishide, H. Photocrosslinked nitroxide polymer cathode-active materials for application in an organic-based paper battery. *Chem. Commun. (Camb. Engl.)* **2007**, *2017*, 1730–1732. [[CrossRef](#)] [[PubMed](#)]
6. Tang, Y.; Zhang, Y.; Li, W.; Ma, B.; Chen, X. Rational material design for ultrafast rechargeable lithium-ion batteries. *Chem. Soc. Rev.* **2015**, *44*, 5926–5940. [[CrossRef](#)] [[PubMed](#)]
7. Arico, A.S.; Bruce, P.; Scrosati, B.; Tarascon, J.-M.; van Schalkwijk, W. Nanostructured materials for advanced energy conversion and storage devices. *Nat. Mater.* **2005**, *4*, 366–377. [[CrossRef](#)]
8. Wu, N.T.; Du, W.Z.; Gao, X.; Zhao, L.; Liu, G.L.; Liu, X.M.; Wu, H.; He, Y.B. Hollow SnO<sub>2</sub> nanospheres with oxygen vacancies entrapped by a N-doped graphene network as robust anode materials for lithium-ion batteries. *Nanoscale* **2018**, *10*, 11460–11466. [[CrossRef](#)] [[PubMed](#)]
9. Whittingham, M.S. Lithium batteries and cathode materials. *Chem. Rev.* **2004**, *104*, 4271–4301. [[CrossRef](#)] [[PubMed](#)]
10. Wang, Y.Y.; Wang, Z.J.; Lei, D.N.; Lv, W.; Zhao, Q.; Ni, B.; Liu, Y.; Li, B.H.; Kang, F.Y.; He, Y.B. Spherical Li Deposited inside 3D Cu Skeleton as Anode with Ultrastable Performance. *ACS Appl. Mater. Interfaces* **2018**, *10*, 20244–20249. [[CrossRef](#)]
11. Zheng, J.C.; Yang, Z.; He, Z.J.; Tong, H.; Yu, W.J.; Zhang, J.F. In situ formed LiNi<sub>0.8</sub>Co<sub>0.15</sub>Al<sub>0.05</sub>O<sub>2</sub>@Li<sub>4</sub>SiO<sub>4</sub> composite cathode material with high rate capability and long cycling stability for lithium-ion batteries. *Nano Energy* **2018**, *53*, 613–621. [[CrossRef](#)]
12. Yan, J.; Liu, X.; Li, B. Recent progress in Li-rich layered oxides as cathode materials for Li-ion batteries. *RSC Adv.* **2014**, *4*, 63268–63284. [[CrossRef](#)]
13. Zhu, C.; Mu, X.; van Aken, P.A.; Maier, J.; Yu, Y. Fast Li Storage in MoS<sub>2</sub>-Graphene-Carbon Nanotube Nanocomposites: Advantageous Functional Integration of 0D, 1D, and 2D Nanostructures. *Adv. Energy Mater.* **2015**, *5*, 1401170. [[CrossRef](#)]
14. Wang, H.; Feng, H.; Li, J. Graphene and Graphene-like Layered Transition Metal Dichalcogenides in Energy Conversion and Storage. *Small* **2014**, *10*, 2165–2181. [[CrossRef](#)] [[PubMed](#)]
15. Liu, J.; Wen, Y.; Wang, Y.; van Aken, P.A.; Maier, J.; Yu, Y. Carbon-Encapsulated Pyrite as Stable and Earth-Abundant High Energy Cathode Material for Rechargeable Lithium Batteries. *Adv. Mater.* **2014**, *26*, 6025–6030. [[CrossRef](#)] [[PubMed](#)]
16. Wang, H.; Liang, Q.; Wang, W.; An, Y.; Li, J.; Guo, L. Preparation of Flower-like SnO<sub>2</sub> Nanostructures and Their Applications in Gas-Sensing and Lithium Storage. *Cryst. Growth Des.* **2011**, *11*, 2942–2947. [[CrossRef](#)]
17. Tang, Y.; Zhang, Y.; Rui, X.; Qi, D.; Luo, Y.; Leow, W.R.; Chen, S.; Guo, J.; Wei, J.; Li, W.; et al. Conductive Inks Based on a Lithium Titanate Nanotube Gel for High-Rate Lithium-Ion Batteries with Customized Configuration. *Adv. Mater.* **2016**, *28*, 1567–1576. [[CrossRef](#)] [[PubMed](#)]
18. Wang, H.; Wu, Y.; Bai, Y.; Zhou, W.; An, Y.; Li, J.; Guo, L. The self-assembly of porous microspheres of tin dioxide octahedral nanoparticles for high performance lithium ion battery anode materials. *J. Mater. Chem.* **2011**, *21*, 10189–10194. [[CrossRef](#)]
19. Liu, Y.; Wei, H.J.; Wang, C.; Wang, F.; Wang, H.C.; Zhang, W.H.; Wang, X.F.; Yan, C.L.; Kim, B.H.; Ren, F.Z. Nitrogen-Doped Carbon Coated WS<sub>2</sub> Nanosheets as Anode for High-Performance Sodium-Ion Batteries. *Front. Chem.* **2018**, *6*, 236. [[CrossRef](#)] [[PubMed](#)]
20. Wang, F.; Liu, Y.; Zhao, Y.F.; Wang, Y.; Wang, Z.J.; Zhang, W.H.; Ren, F.Z. Facile Synthesis of Two-Dimensional Porous MgCo<sub>2</sub>O<sub>4</sub> Nanosheets as Anode for Lithium-Ion Batteries. *Appl. Sci.* **2018**, *8*, 22. [[CrossRef](#)]
21. Liu, G.L.; Cui, J.; Luo, R.J.; Liu, Y.; Huang, X.X.; Wu, N.T.; Jin, X.Y.; Chen, H.P.; Tang, S.Y.; Kim, J.K.; et al. 2D MoS<sub>2</sub> grown on biomass-based hollow carbon fibers for energy storage. *Appl. Surf. Sci.* **2019**, *469*, 854–863. [[CrossRef](#)]

22. Liu, G.; Liu, X.; Li, X.; Jin, X.; Xiao, H.; Wu, N.; Guo, D.; Tang, S. Coordination Engineering Construction of Si@ZnS@N,S-Doped Reduced Graphene Oxide Nanocomposite as Anode Material with Enhanced Lithium Storage Performance. *Energy Technol.* **2019**, *7*, 1900186. [[CrossRef](#)]
23. Zhou, X.; Zhang, Z.; Lu, X.; Lv, X.; Ma, G.; Wang, Q.; Lei, Z. Sb<sub>2</sub>O<sub>3</sub> Nanoparticles Anchored on Graphene Sheets via Alcohol Dissolution-Reprecipitation Method for Excellent Lithium-Storage Properties. *ACS Appl. Mater. Interfaces* **2017**, *9*, 34927–34936. [[CrossRef](#)] [[PubMed](#)]
24. Wang, J.X.; Li, W.; Wang, F.; Xia, Y.Y.; Asiri, A.M.; Zhao, D.Y. Controllable synthesis of SnO<sub>2</sub>@C yolk-shell nanospheres as a high-performance anode material for lithium ion batteries. *Nanoscale* **2014**, *6*, 3217–3222. [[CrossRef](#)] [[PubMed](#)]
25. Tan, Y.; Chen, L.; Chen, H.; Hou, Q.; Chen, X. Synthesis of a symmetric bundle-shaped Sb<sub>2</sub>O<sub>3</sub> and its application for anode materials in lithium ion batteries. *Mater. Lett.* **2018**, *212*, 103–106. [[CrossRef](#)]
26. Hong, K.S.; Nam, D.H.; Lim, S.J.; Sohn, D.; Kim, T.H.; Kwon, H. Electrochemically Synthesized Sb/Sb<sub>2</sub>O<sub>3</sub> Composites as High-Capacity Anode Materials Utilizing a Reversible Conversion Reaction for Na-Ion Batteries. *ACS Appl. Mater. Interfaces* **2015**, *7*, 17264–17271. [[CrossRef](#)] [[PubMed](#)]
27. Hu, M.J.; Jiang, Y.Z.; Sun, W.P.; Wang, H.T.; Jin, C.H.; Yan, M. Reversible Conversion-Alloying of Sb<sub>2</sub>O<sub>3</sub> as a High-Capacity, High-Rate, and Durable Anode for Sodium Ion Batteries. *ACS Appl. Mater. Interfaces* **2014**, *6*, 19449–19455. [[CrossRef](#)]
28. Zhou, X.Z.; Zhang, Z.F.; Wang, J.W.; Wang, Q.T.; Ma, G.F.; Lei, Z.Q. Sb<sub>2</sub>O<sub>4</sub>/reduced graphene oxide composite as high-performance anode material for lithium ion batteries. *J. Alloys Compd.* **2017**, *699*, 611–618. [[CrossRef](#)]
29. Zhou, X.Z.; Zhang, Z.F.; Xu, X.H.; Yan, J.; Ma, G.F.; Lei, Z.Q. Anchoring Sb<sub>6</sub>O<sub>13</sub> Nanocrystals on Graphene Sheets for Enhanced Lithium Storage. *ACS Appl. Mater. Interfaces* **2016**, *8*, 35398–35406. [[CrossRef](#)]
30. Deng, M.X.; Li, S.J.; Hong, W.W.; Jiang, Y.L.; Xu, W.; Shuai, H.L.; Zou, G.Q.; Hu, Y.C.; Hou, H.S.; Wang, W.L.; et al. Octahedral Sb<sub>2</sub>O<sub>3</sub> as high-performance anode for lithium and sodium storage. *Mater. Chem. Phys.* **2019**, *223*, 46–52. [[CrossRef](#)]
31. Gao, H.; Zhou, W.; Jang, J.-H.; Goodenough, J.B. Cross-Linked Chitosan as a Polymer Network Binder for an Antimony Anode in Sodium-Ion Batteries. *Adv. Energy Mater.* **2016**, *6*, 1502130. [[CrossRef](#)]
32. Pan, J.; Wang, N.; Zhou, Y.; Yang, X.; Zhou, W.; Qian, Y.; Yang, J. Simple synthesis of a porous Sb/Sb<sub>2</sub>O<sub>3</sub> nanocomposite for a high-capacity anode material in Na-ion batteries. *Nano Res.* **2017**, *10*, 1794–1803. [[CrossRef](#)]
33. Nam, D.-H.; Hong, K.-S.; Lim, S.-J.; Kim, M.-J.; Kwon, H.-S. High-Performance Sb/Sb<sub>2</sub>O<sub>3</sub> Anode Materials Using a Polypyrrole Nanowire Network for Na-Ion Batteries. *Small* **2015**, *11*, 2885–2892. [[CrossRef](#)] [[PubMed](#)]
34. Fei, J.; Cui, Y.; Li, J.; Xu, Z.; Yang, J.; Wang, R.; Cheng, Y.; Hang, J. A flexible Sb<sub>2</sub>O<sub>3</sub>/carbon cloth composite as a free-standing high performance anode for sodium ion batteries. *Chem. Commun.* **2017**, *53*, 13165–13167. [[CrossRef](#)] [[PubMed](#)]
35. Li, D.; Yana, D.; Ma, J.; Qin, W.; Zhang, X.; Lu, T.; Pan, L. One-step microwave-assisted synthesis of Sb<sub>2</sub>O<sub>3</sub>/reduced graphene oxide composites as advanced anode materials for sodium-ion batteries. *Ceram. Int.* **2016**, *42*, 15634–15642. [[CrossRef](#)]
36. Liu, Y.; Tai, Z.; Zhou, T.; Sencadas, V.; Zhang, J.; Zhang, L.; Konstantinov, K.; Guo, Z.; Liu, H.K. An All-Integrated Anode via Interlinked Chemical Bonding between Double-Shelled-Yolk-Structured Silicon and Binder for Lithium-Ion Batteries. *Adv. Mater.* **2017**, *29*, 1703028. [[CrossRef](#)] [[PubMed](#)]
37. Koo, B.; Kim, H.; Cho, Y.; Lee, K.T.; Choi, N.S.; Cho, J. A Highly Cross-Linked Polymeric Binder for High-Performance Silicon Negative Electrodes in Lithium Ion Batteries. *Angew. Chem. Int. Ed.* **2012**, *51*, 8762–8767. [[CrossRef](#)] [[PubMed](#)]
38. Wei, Y.; Wang, Z.; Ye, H.; Mou, J.; Lei, D.; Liu, Y.; Lv, W.; Li, B.; Kang, F.; He, Y.-B. A Stable Cross-Linked Binder Network for SnO<sub>2</sub> Anode with Enhanced Sodium-Ion Storage Performance. *ChemistrySelect* **2017**, *2*, 11365–11369. [[CrossRef](#)]
39. Song, J.X.; Zhou, M.J.; Yi, R.; Xu, T.; Gordin, M.L.; Tang, D.H.; Yu, Z.X.; Regula, M.; Wang, D.H. Interpenetrated Gel Polymer Binder for High-Performance Silicon Anodes in Lithium-ion Batteries. *Adv. Funct. Mater.* **2014**, *24*, 5904–5910. [[CrossRef](#)]
40. Rohan, R.; Kuo, T.C.; Chiou, C.Y.; Chang, Y.L.; Li, C.C.; Lee, J.T. Low-cost and sustainable corn starch as a high-performance aqueous binder in silicon anodes via in situ cross-linking. *J. Power Sources* **2018**, *396*, 459–466. [[CrossRef](#)]

41. Chevrier, V.L.; Ceder, G. Challenges for Na-ion Negative Electrodes. *J. Electrochem. Soc.* **2011**, *158*, A1011–A1014. [[CrossRef](#)]
42. Vukovic, M.; Brankovic, Z.; Poleti, D.; Recnik, A.; Brankovic, G. Novel simple methods for the synthesis of single-phase valentinite Sb<sub>2</sub>O<sub>3</sub>. *J. Sol-Gel Sci. Technol.* **2014**, *72*, 527–533. [[CrossRef](#)]
43. Shi, Y.T.; Lv, W.; Niu, S.Z.; He, Y.B.; Zhou, G.M.; Chen, G.H.; Li, B.H.; Yang, Q.H.; Kang, F.Y. A Carbon-Sulfur Hybrid with Pomegranate-like Structure for Lithium-Sulfur Batteries. *Chem. Asian J.* **2016**, *11*, 1343–1347. [[CrossRef](#)] [[PubMed](#)]
44. Chou, Y.H.; Cundy, C.S.; Garforth, A.A.; Zholobenko, V.L. Mesoporous ZSM-5 catalysts: Preparation, characterisation and catalytic properties. Part I: Comparison of different synthesis routes. *Microporous Mesoporous Mater.* **2006**, *89*, 78–87. [[CrossRef](#)]
45. Wang, L.; Wang, D.; Zhang, F.X.; Jin, J. Interface Chemistry Guided Long-Cycle-Life Li-S Battery. *Nano Lett.* **2013**, *13*, 4206–4211. [[CrossRef](#)] [[PubMed](#)]
46. Xue, M.Z.; Fu, Z.W. Electrochemical reaction of lithium with nanostructured thin film of antimony trioxide. *Electrochem. Commun.* **2006**, *8*, 1250–1256. [[CrossRef](#)]
47. Hou, H.S.; Jing, M.J.; Yang, Y.C.; Zhang, Y.; Zhu, Y.R.; Song, W.X.; Yang, X.M.; Ji, X.B. Sb porous hollow microspheres as advanced anode materials for sodium-ion batteries. *J. Mater. Chem. A* **2015**, *3*, 2971–2977. [[CrossRef](#)]
48. Jin, J.; Huang, S.Z.; Shu, J.; Wang, H.E.; Li, Y.; Yu, Y.; Chen, L.H.; Wang, B.J.; Su, B.L. Highly porous TiO<sub>2</sub> hollow microspheres constructed by radially oriented nanorods chains for high capacity, high rate and long cycle capability lithium battery. *Nano Energy* **2015**, *16*, 339–349. [[CrossRef](#)]
49. Bao, W.Z.; Liu, L.; Wang, C.Y.; Choi, S.; Wang, D.; Wang, G.X. Facile Synthesis of Crumpled Nitrogen-Doped MXene Nanosheets as a New Sulfur Host for Lithium-Sulfur Batteries. *Adv. Energy Mater.* **2018**, *8*, 1702485. [[CrossRef](#)]
50. Gao, P.; Zhang, C.F.; Wen, G.W. Equivalent circuit model analysis on electrochemical impedance spectroscopy of lithium metal batteries. *J. Power Sources* **2015**, *294*, 67–74. [[CrossRef](#)]
51. Yang, X.; Ma, J.J.; Wang, H.J.; Chai, Y.Q.; Yuan, R. Partially reduced Sb/Sb<sub>2</sub>O<sub>3</sub>@C spheres with enhanced electrochemical performance for lithium ion storage. *Mater. Chem. Phys.* **2018**, *213*, 208–212. [[CrossRef](#)]
52. Wang, Z.M.; Cheng, Y.; Li, Q.; Chang, L.M.; Wang, L.M. Facile synthesis of one-dimensional hollow Sb<sub>2</sub>O<sub>3</sub>@TiO<sub>2</sub> composites as anode materials for lithium ion batteries. *J. Power Sources* **2018**, *389*, 214–221. [[CrossRef](#)]
53. Zhou, J.; Zheng, C.; Wang, H.; Yang, J.; Hu, P.; Guo, L. 3D nest-shaped Sb<sub>2</sub>O<sub>3</sub>/RGO composite based high-performance lithium-ion batteries. *Nanoscale* **2016**, *8*, 17131–17135. [[CrossRef](#)] [[PubMed](#)]

